Journal of Materials Chemistry A

PAPER

View Article Online
View Journal | View Issue

Cite this: J. Mater. Chem. A, 2016, 4, 10964

Enhanced conversion reaction kinetics in low crystallinity SnO_2/CNT anodes for Na-ion batteries†

Jiang Cui,[ab] Zheng-Long Xu,[a] Shanshan Yao,[a] Jiaqiang Huang,[a] Jian-Qiu Huang,[a] Sara Abouali,[a] Mohammad Akbari Garakani,[a] Xiaohui Ning*[b] and Jang-Kyo Kim*[a]

Received 28th April 2016
Accepted 17th June 2016

DOI: 10.1039/c6ta03541h

www.rsc.org/MaterialsA

The specific capacities of SnO_2 anodes in sodium ion batteries (SIBs) are far below the values expected from theory. Herein, we propose that the kinetically-controlled, reversible 'conversion reaction' between Na ions and SnO_2 is responsible for Na ion storage in SnO_2 anodes where the ion diffusion rate is the limiting factor. This revelation is contrary to the current understanding of the 'alloying reaction' as the major reaction process. Aiming to fully utilize the theoretical capacity from the conversion reaction, a composite electrode consisting of carbon nanotubes coated with a mainly amorphous SnO_2 phase together with crystalline nanoparticles is synthesized. The SnO_2/CNT anodes deliver a superior specific capacity of 630.4 mA h g^{-1} at 0.1 A g^{-1} and 324.1 mA h g^{-1} at a high rate of 1.6 A g^{-1} due to the enhanced kinetics. The volume expansion of the composite is accommodated by the CNT substrate, giving rise to an excellent 69% capacity retention after 300 cycles. The aforementioned findings give new insight into the fundamental understanding of the electrochemical kinetics of SnO_2 electrodes and offer a potential solution to the low capacity and poor cyclic stability of other metal oxide anodes based on conversion reactions.

1. Introduction

Since their first commercialization two decades ago, lithium ion batteries (LIBs) currently dominate the rechargeable batteries market, especially for portable electronic devices and electric vehicles (EVs).[1,2] With the rapid expansion of these markets, however, there has been increasing demand to develop batteries with much reduced manufacturing costs and better materials. As a potential alternative to LIBs, sodium ion batteries (SIBs) have drawn much attention due to the low cost of sodium sources and their similar working principles to LIBs.[3–6] Apart from the successful development of stable cathode materials, the synthesis of anode materials possessing high capacities and long cyclic life has become the biggest challenge for SIBs.[7,8]

Although graphite has been widely employed as an anode in LIBs, it has limited capacity in SIBs because it has unfavorable energetics and the large radius of Na ions makes them difficult to intercalate into graphite layers.[9–11] SnO_2 has been considered one of the most promising anode materials both for LIBs and SIBs with a much higher theoretical capacity than graphite anodes, and hence has attracted much research interest.[12–16] In particular, SnO_2-based nanocomposites hybridized with nanocarbon materials like graphene, carbon nanofibers and porous carbon, have shown many advantages.[17–30] However, the measured specific capacities of SnO_2 in most of the above studies remained below 400 mA h g^{-1} with a low initial coulombic efficiency of about 30%, although its theoretical capacity is as high as 1378 mA h g^{-1}.[24] If both the conversion and alloying reactions given by eqn (1) and (2), respectively, were made reversible, a capacity closer to the theoretical value should be achieved, as in resent studies on LIBs.[31–34] Thus, more effort is needed to gain an in-depth understanding of these limited electrochemical reactions.

$$SnO_2 + 4Na^+ + 4e^- \rightleftarrows 2Na_2O + Sn \quad (1)$$

$$Sn + xNa^+ + xe^- \rightleftarrows Na_xSn\ (x \leq 3.75) \quad (2)$$

The excellent energy storage behavior of SnO_2 anodes in LIBs has inspired us to explore how existing issues can be resolved. There are three main issues that need to be addressed to enhance the performance of SnO_2 in SIBs. (i) Slow electrochemical reaction kinetics of SnO_2 with Na ions, resulting in irreversible conversion reactions. This irreversible capacity loss is also responsible for the low initial coulombic efficiency.[35] (ii) Intrinsic difficulties for the Na–Sn alloying reaction to take place with a limited capacity arising from alloying reactions alone.[20,27,36] (iii) The introduction of large volume expansion

[a]Department of Mechanical and Aerospace Engineering, The Hong Kong University of Science and Technology, Clear Water Bay, Hong Kong, P. R. China. E-mail: mejkkim@ust.hk

[b]Center for Advancing Materials Performance from the Nanoscale (CAMP-Nano), State Key Laboratory for Mechanical Behavior of Materials, Xi'an Jiaotong University, Xi'an 710049, P. R. China. E-mail: xiaohuining@mail.xjtu.edu.cn

† Electronic supplementary information (ESI) available: TGA, DSC and XRD fitting curves of A-SnO_2/CNT; FTIR spectrum of A-SnO_2/CNT; CV curves of C-SnO_2/CNT; electrochemical performance tested at 0.1 A g^{-1}; comparison of cyclic and rate performance among SnO_2 based anodes; real time video of sodiation captured through *in situ* TEM. See DOI: 10.1039/c6ta03541h

during sodiation, causing rapid decay of capacity and eventual failure of the electrode.[37,38] To resolve the above issues, the SnO_2 electrodes should be designed in such a way as to enhance the reaction kinetics and minimize the volume expansion. An effective option is to incorporate carbon nanotubes (CNTs) both as the conductive substrate of SnO_2 and as a buffer to accommodate the volume expansion.[23,26,39] The incorporation of CNTs enhanced the specific capacities and capacity retention because of the improved electronic conduction and reduced electron/ion transfer resistance. However, the electrical contact between the large SnO_2 particles and the CNT surface needed further improvement to overcome the poor kinetics which limited the widespread application of SnO_2/CNT electrodes in SIBs.

In this study, a thin layer of well-dispersed SnO_2 particles is uniformly coated on CNTs. A low temperature route allows the synthesis of a mainly amorphous SnO_2 phase with a much shortened solid-state diffusion path for facile Na ion transport. The p–n heterojunctions induced by the interactions between the SnO_2 particles and CNT substrate also reduce the energy barrier and facilitate charge transfer, leading to a better Na storage capability.[40–42] Such interactions have been shown to not only immobilize SnO_2 nanoparticles on CNTs but also to improve the conductivity of SnO_2,[40] favouring enhanced electron transfer.[41] The underlying electrochemical reaction mechanisms and kinetics are probed to offer an insightful view to designing better SnO_2-based electrodes for SIBs.

2. Experimental section

2.1 Synthesis of SnO_2/CNT composites

CNTs coated with mainly amorphous SnO_2 particles were synthesized through a facile $SnCl_2$ solution-based precipitation method as illustrated in Fig. 1. Typically, multi-walled CNTs (with an average diameter of 50 nm and 10 μm in length, supplied by Shenzhen Nanotech) were refluxed in 40% nitric acid at 110 °C for 2 h to remove any impurities and to functionalize the CNT surface.[43] 10 mg of functionalized CNTs were dispersed in 40 mL of deionized (DI) water using sonication for 30 min to form a homogeneous mixture. 0.5 g of $SnCl_2 \cdot 2H_2O$ was added to the above mixture with vigorous stirring for 2 h at room temperature to allow the hydrolysis reaction. The solid products were collected using vacuum filtration and washed with DI water to remove unreacted $SnCl_2$, followed by drying at 60 °C for 8 h. The final product was designated as A (amorphous)-SnO_2/CNT. A-SnO_2/CNT was calcined at 500 °C for 4 h in a tube furnace with a nitrogen flow to fully crystalize SnO_2, which was designated as C (crystalline)-SnO_2/CNT.

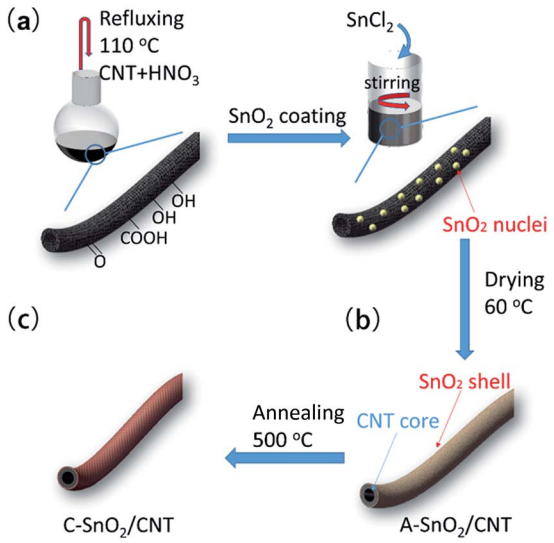

Fig. 1 Schematic representation of the synthesis of SnO_2/CNT nanocomposites: (a) pre-treatment of CNTs; (b) nucleated ultrafine, mainly amorphous SnO_2/CNT (A-SnO_2/CNT); and (c) crystalline SnO_2/CNT (C-SnO_2/CNT) obtained after annealing.

2.2 Material characterization

The structures of the SnO_2/CNT composites were characterized using powder X-ray diffraction analysis (XRD, PW1830, Philips) with Cu Kα radiation from 20° to 80°. The morphologies of the composites were examined using scanning electron microscopy (SEM, JOEL 6700F) and transmission electron microscopy (TEM, JOEL 2010). The chemical groups on the samples were characterized using Fourier transform infra-red spectroscopy (FTIR, Vertex 70 Hyperion 1000). To identify their chemical status, X-ray photoelectron spectroscopy (XPS, Surface analysis PHI5600, Physical Electronics) with an Al Kα excitation source was employed. Thermogravimetric analysis (TGA, Q5000) was used to evaluate the compositions at a heating rate of 10 °C min^{-1} from 25 to 800 °C in air. The heat flow was characterized on a differential scanning calorimetry system (DSC, 92 Setaram).

2.3 Electrochemical tests

To prepare the electrode, the active material was mixed with Super P and carboxymethyl cellulose (CMC) binder in a weight ratio of 60 : 20 : 20 with DI water as solvent to form a uniform slurry. The slurry was coated onto copper foil, from which disks of 12 mm in diameter were cut. CR2032 half cells were assembled in an argon filled glove box. Sodium foil was used as the counter electrode, and the electrolyte was prepared using 1 M $NaClO_4$ dissolved in propylene carbonate (PC) and ethyl carbonate (EC) (1 : 1 by volume) along with 5 wt% of fluoroethylene carbonate (FEC) additive, while glass fibers (Whatman, GF/D) were used as the separator.

Galvanostatic charge/discharge (GCD) tests were conducted on a battery testing system (Land 2001CT) in the potential range of 0.005–3.0 V and at different current densities. The specific capacity was calculated based on the total weight of the SnO_2/CNT composite. Cyclic voltammetry (CV) tests were performed at scan rates varying from 0.1 to 5 mV s^{-1} between 0.005 and 3.0 V on an electrochemical workstation (CHI 660C). Electrochemical impedance spectra (EIS) were obtained in the frequency range 0.1–10^5 Hz on the same workstation.

2.4 *In situ* TEM examination

To obtain an insight into the sodiation/desodiation mechanisms and the evolution of the structures, *in situ* TEM was carried out using an STM holder (Nanofactory), similar to our previous work.[44]

The active material was attached to the tip of a Cu wire as the working electrode, while Na metal was loaded onto the tip of another Cu wire as the counter electrode. The Na metal was naturally oxidized in air to form a layer of Na_2O and NaOH mixture when the holder was transferred to the TEM chamber, which later served as the solid electrolyte. A potentiostat was used to apply the overpotential to the electrode to drive the diffusion of Na ions.

3. Results and discussion

3.1 Structure and morphology

According to previous studies,[45,46] Sn^{2+} ions in water at a high concentration become easily oxidized to form SnO_2 nanoparticles with diameters less than 10 nm. If nanocarbons, such as functionalized CNTs or graphene oxide containing oxygenated functional groups, are added into the solution, they serve as the nucleation sites on which SnO_2 coating is uniformly grown.[47,48] Typical SEM and TEM images of pristine CNTs, A-SnO_2/CNT and C-SnO_2/CNT are shown in Fig. 2. The morphologies of A-SnO_2/CNT and C-SnO_2/CNT (Fig. 2b and c) were similar to the pristine CNTs (Fig. 2a), except the increase in diameter from 50 to 60–70 nm due to the deposition of SnO_2 coating. The TEM images (Fig. 2d–f) indicate that the SnO_2 coating in A-SnO_2/CNT obtained before calcination consisted of a mainly amorphous phase, presumably in the form of subnano-sized particles[49] as well as ordered/disordered crystallites of 2–5 nm in diameter. The SAED pattern (inset of Fig. 2f) offered another solid piece of evidence: the broad space between the (110) and (101) diffraction rings suggests the existence of long-range disordered SnO_2.[49,50] In contrast, the SnO_2 particles in the C-SnO_2/CNT composites (Fig. 2g and h) were highly crystalline with enlarged diameters ranging from 5–10 nm due to particle growth during calcination, as indicated by the white circles in Fig. 2i. The sharp diffraction points in the inset of Fig. 2i further prove that the thermal treatment was responsible for the formation and growth of SnO_2 crystals.

The TGA and DSC curves shown in Fig. S1† provide information on the composition of A-SnO_2/CNT. The gradual weight reduction from room temperature to 400 °C in the TGA curve corresponds to the removal of both moisture and the oxygen functional groups on the CNTs. The weight suddenly dropped between 470 and 630 °C due to the decomposition of CNTs in air, giving a net CNT weight of ~16 wt%, while the remaining 72 wt% is attributed to SnO_2. The DSC curve measured from ambient temperature to 350 °C showed an endothermic peak located at ~100 °C, corresponding to evaporation of moisture from the composites, and an exothermic peak at ~300 °C is likely due to the heat released during crystallization of the long-range disordered SnO_2 coating.

The structure and chemical status of the SnO_2/CNT composites were evaluated using XRD and XPS, as shown in Fig. 3. There were no prominent peaks in the XRD spectrum of A-SnO_2/CNT except for two broad, high intensity areas at 2θ = 22–36° and 48–56° (Fig. 3a), evidence of low crystallinity.[51] The corresponding fitted XRD profiles of the (110), (101) and (211) planes are shown in Fig. S2.† The Gaussian function was used to fit and calculate the areas of the crystalline and amorphous sectors of the peaks using commercial Jade software, finding 14.7% crystallinity according to the calculated result given by the software.[52] Notably, the highest intensity peak located at 2θ = ~26.5° representing the (110) face of SnO_2 marginally downshifted from the standard PDF card as a result of an enlarged lattice *d*-spacing from the standard value of 3.3470 to 3.3504 Å, which is favorable for enhancing ion diffusion rates. In contrast, four prominent peaks were observed for C-SnO_2/CNT, all of which refer to rutile SnO_2 (PDF #70-4177). This finding confirmed the growth of SnO_2 particles to full crystals during the annealing process of A-SnO_2/CNT, in agreement with the TEM results (Fig. 2).

It is well known that SnO_2 and SnO respond differently during electrochemical reactions in SIBs,[20] making it important to determine the exact chemical status of Sn in A-SnO_2/CNT. However, the information obtained from the XRD analysis was rather inconclusive due to the relatively low crystallinity. It is interesting to note that the general XPS spectra given in Fig. 3b showed almost identical profiles for both the A- and C-SnO_2/CNT composites. Indeed, the deconvoluted Sn3d spectra (Fig. 3c) presented identical, prominent $Sn3d_{5/2}$ and $Sn3d_{5/2}$ peaks centered at 487.5 and 496 eV, respectively, for both composites. These binding energies are attributed to Sn^{4+}, with virtually no Sn^{2+} or Sn,[53] confirming SnO_2 was in both composites. Various functional groups were identified from the deconvoluted C1s spectra, as shown in Fig. 3d. Five peaks were detected, including C_g sp^2 hybridization at 284.5 eV, C_d sp^3 hybridization at 285.1 eV, C–O at 286.2 eV, C═O at 287.5 eV and O–C═O at 288.9 eV. The existence of these functional groups was also confirmed using FTIR spectrum (Fig. S3†). The C_g sp^2 and C_d sp^3 peaks are attributed to the chemical bonds among the carbon atoms and defects in CNTs, respectively, while the C–O, C═O and O–C═O peaks are attributed to the oxygenated functional groups attached to the CNTs.[54,55] They helped not only the uniform dispersion of the CNTs in the precursor solution, but also the formation of the SnO_2 layer on the CNTs.

3.2 Electrochemical performance

Although a few proposals have been put forward to explain the electrochemical reaction mechanisms between SnO_2 and Na ions, similar to Li ion storage in LIBs (see Introduction), there is a lack of solid evidence to account for what really happens during these reactions.[27,28] Therefore, the results from the cyclic voltammetry (CV), *ex situ* XRD analysis and *in situ* TEM examination (to be discussed in Section 3.4) are combined here to reveal the phase changes of SnO_2 during the electrochemical reaction with Na ions. The CV curve of the first cathodic cycle, shown in Fig. 4a, exhibited a prominent peak located at 0.25 V

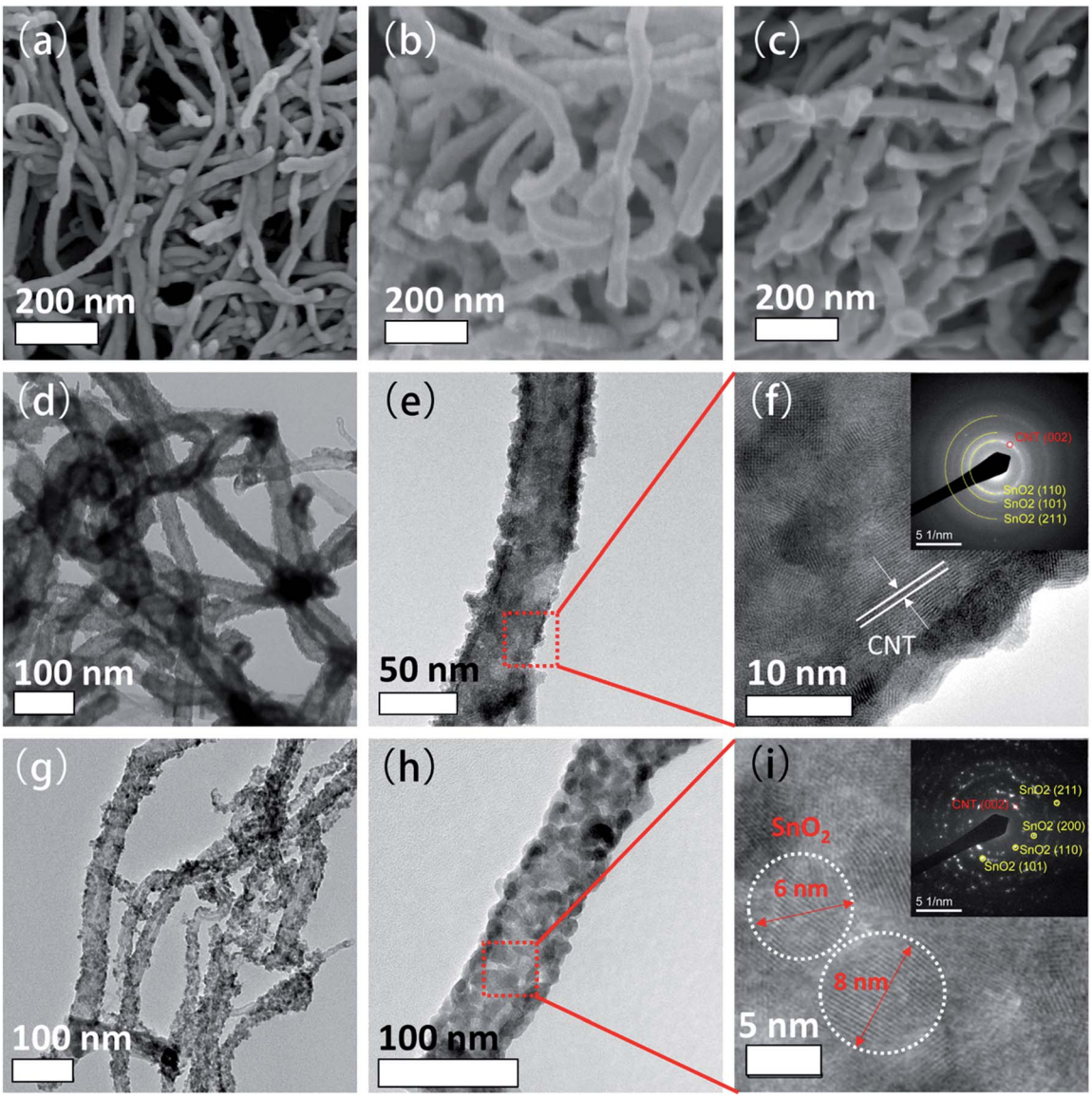

Fig. 2 (a–c) SEM images of pristine CNTs, A-SnO_2/CNT and C-SnO_2/CNT composites; (d–f) TEM images of A-SnO_2/CNT composites with SAED pattern in the inset of f; (g–i) TEM images of C-SnO_2/CNT composites with SAED pattern in the inset of (i).

and two low peaks centered at 0.79 and 1.05 V, a reflection of the continuous formation of SEI layers in the wide voltage range. The two small peaks disappeared in the following cycles, indicating the completion of the SEI layer formation in the first cycle. Therefore, in the following 2^{nd} and 3^{rd} cycles, only the prominent cathodic peak remained while the corresponding potential shifted to 0.3 V due to activation of the electrode. The strong anodic peak centered at 1.35 V persisted throughout all the cycles, which warrants a special mention because this has never been reported previously for SnO_2 electrodes in SIBs. Because the neat CNTs contributed only a negligible capacity of less than 10 mA h g^{-1} to the composite electrode due to the intrinsic difficulties for Na intercalation (Fig. S4†) and showed no distinct peak in the anodic scan (Fig. S5†), we propose here that the peak corresponds to the conversion reaction of SnO_2 during desodiation, which may contribute to the majority of the battery capacity in view of its large area covering over 80% of the whole anodic curve, as explained below.

The corresponding GCD curves of the A-SnO_2/CNT electrode for the 1^{st}, 2^{nd}, 50^{th} and 100^{th} cycles are given in Fig. 4b. Following the high initial discharge capacity of 1106.6 mA h g^{-1}, the electrode exhibited a reversible specific capacity of 630.4 mA h g^{-1}. Considering the capacity contribution of ~30 mA h g^{-1} from 20 wt% Super P according to Fig. S4,† the remaining capacity was still higher than the majority of previous reports on SnO_2 anodes (Fig. S6 and Table S1†). The GCD curves here showed slopes instead of constant voltage plateaus due to the nanosize effect.[56] However, gradient changes of the slopes were observed at ~0.3 and ~1.35 V in the discharge and charge curves, respectively, which are ascribed to reversible reactions between SnO_2 and the Na ions, in agreement with the CV results (Fig. 4a). Of note is that the coulombic efficiency of the first

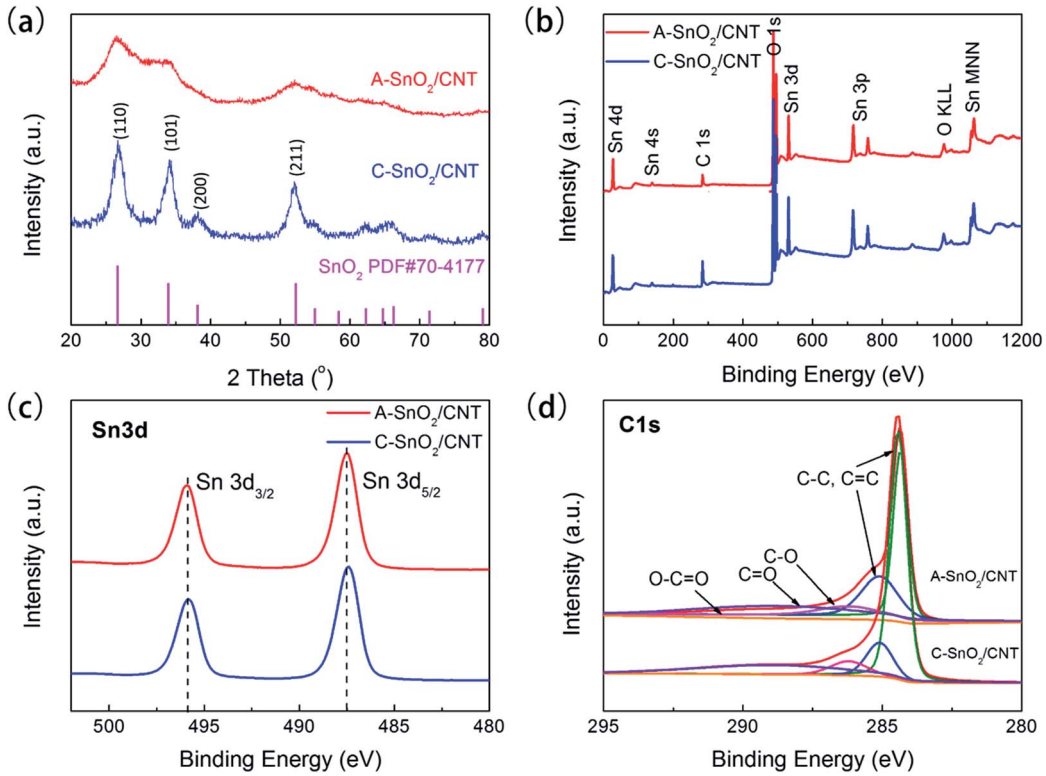

Fig. 3 (a) XRD patterns, (b) general XPS spectra, and deconvoluted XPS spectra of (c) Sn3d and (d) C1s of A-SnO_2/CNT and C-SnO_2/CNT composites.

cycle reached 57%, much higher than ~40% for other SnO_2 anodes.[35] The coulombic efficiency here is an important parameter determining the battery performance by reflecting the reversibility of the conversion reactions given by eqn (1). Recent studies[34,49] demonstrated that the simultaneous conversion and alloying reactions in SnO_2 electrodes enhanced the Li ion storage performance with a remarkable capacity over 1400 mA h g^{-1}, beyond the known theoretical capacity of SnO_2 anodes for LIBs. Furthermore, it is found that the reversible conversion reaction took place only when the SnO_2 particles with a diameter less than 10 nm were uniformly dispersed on a conductive supporting matrix, like CNTs, carbon nanofibers (CNFs) or graphene sheets.[49] Similar to LIBs, the A-SnO_2/CNT composites consisting of a uniform and thin SnO_2 layer on the CNTs satisfied the above requirement, giving rise to a high coulombic efficiency in SIBs. The synergy arising from the uniform SnO_2 layer, the enlarged lattice distance of SnO_2 due to its mainly amorphous nature, and the highly conductive CNTs contributed positively to the reaction kinetics which played an important role in enhancing the electrochemical performance.

Unlike in LIBs, the alloying reaction between the Sn crystals embedded in the Na_2O matrix and the Na ions from the electrolyte (eqn (2)) is unlikely to take place due to the high energy barrier of the reaction process. This hypothesis was partly confirmed from the *ex situ* XRD analysis (Fig. 4c) conducted at different potential stages of the CV tests, which are labeled as A, B and C (Fig. 4a). When the battery was fully discharged to 0 V, apart from the Cu and CuO peaks stemming from the copper foil used as the current collector, four prominent peaks corresponding to α-Sn and β-Sn appeared (Fig. 4c-A). However, no obvious peaks indicative of a Sn–Na alloy were found, verifying the above hypothesis. When the battery was recharged to 0.8 V, the Sn peaks remained with only marginal changes in peak intensity (Fig. 4c-B), indicating that Sn and Na_2O hardly reacted at a charging voltage below 0.8 V. When the electrode was further charged to 2 V, the Sn peaks all disappeared, and instead a broad peak corresponding to SnO_2 emerged at 2θ = ~26° (Fig. 4c-C). This observation proves that the conversion reaction given by eqn (1) occurred in the voltage range 0.8–2 V. In summary, the conversion reaction of eqn (1) was responsible for the anodic peak in the CV curve, which would in turn contribute to the vast majority of the capacity of amorphous SnO_2 electrodes.

The rate performances of the two electrodes are shown in Fig. 4d. It is worth noting that the A-SnO_2/CNT electrode presented consistently – by at least 250–300 mA h g^{-1} – higher specific capacities than the C-SnO_2/CNT electrode for all current densities studied, ranging from 0.1–1.6 A g^{-1}. The former electrode delivered reversible specific capacities of 630.4 and 324.1 mA h g^{-1} at 0.1 and 1.6 A g^{-1}, respectively, confirming it as a promising anode for SIBs. The corresponding reversible capacities for the latter electrode were 325 and 50 mA h g^{-1}. The relatively poor Na ion storage behavior of the C–SnO_2/CNT electrode appears to be associated with three major reasons. (i) The size growth of SnO_2 inevitably extended the Na ion diffusion length, deteriorating the electrochemical performance. (ii)

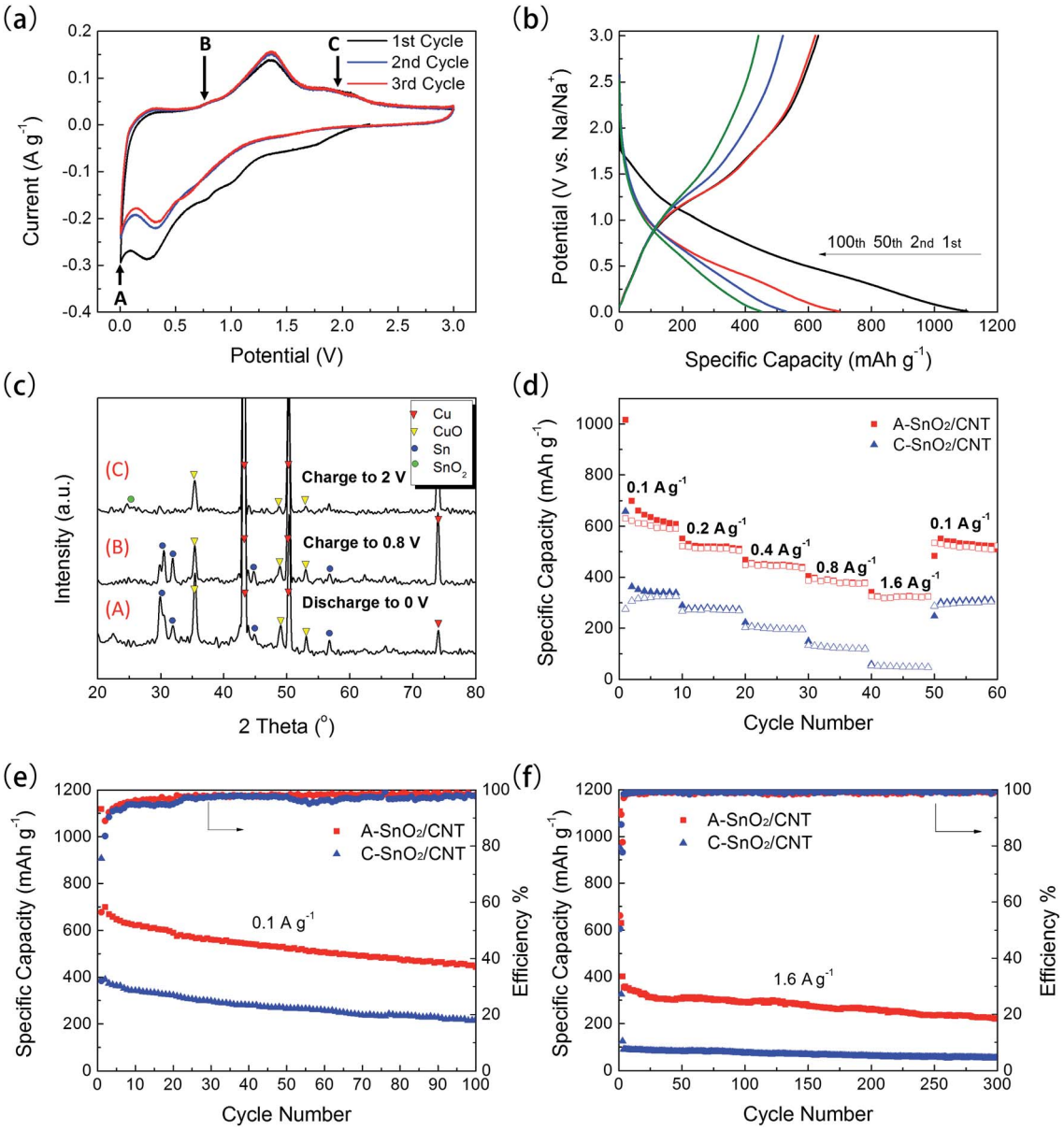

Fig. 4 (a) CV curves of the A-SnO_2/CNT electrode at a scan rate of 0.1 mV s^{-1}; (b) galvanostatic charge/discharge profiles of the A-SnO_2/CNT electrode between 0.005 V and 3 V at 0.1 A g^{-1}; (c) *ex situ* XRD spectra of the A-SnO_2/CNT electrode obtained at different stages; (d) rate capacities, and (e) cyclic performance of the A- and C-SnO_2/CNT electrodes at 0.1 A g^{-1}; and (f) long cycle test of the A- and C-SnO_2/CNT electrodes at 1.6 A g^{-1}.

The ordered crystal surfaces formed upon full crystallization hindered the diffusion and intercalation of Na ions.[35] (iii) The size growth associated with full crystallization of the SnO_2 particles weakened the interaction between SnO_2 and the CNTs due to fewer surface atoms of SnO_2.[40] Details of Na ion diffusion and the charge transfer kinetics are discussed in the following sections.

Cyclic tests were conducted at 0.1 A g^{-1} and 1.6 A g^{-1} in the voltage range from 5 mV to 3 V, as shown in Fig. 4e and f. The A-SnO_2/CNT composite electrode delivers a much higher capacity than both the neat SnO_2 and neat CNT electrodes (Fig. S4†) when measured at the same current density of 0.1 A g^{-1} confirming the aforementioned synergistic effect. Furthermore, after the initial 20 cycles of activation, the coulombic efficiencies of both electrodes tested at 1.6 A g^{-1} reached 98%, indicating excellent reversibility. When the cell finished 300 cycles, the A-SnO_2/CNT electrode maintained 223.2 mA h g^{-1}, equivalent to 69% of the initial capacity of 324 mA h g^{-1} with a capacity reduction of 0.1% per cycle. However, the C-SnO_2/CNT electrode presented a specific capacity of less than 50 mA h g^{-1} after 300 cycles due to the poor reaction kinetics.

3.3 Sodium ion storage kinetics

It is well known that both electrons and Na ions are difficult to transport in SnO_2 in a phenomenon called 'slow

electrochemical reaction kinetics'. A few new features were introduced to enhance the reaction kinetics in the design of the current A-SnO_2/CNT composite electrode: *e.g.* (i) shortening the diffusion path by making the particle size smaller, (ii) accelerating the diffusion rate by enlarging the lattice distance of SnO_2 and (iii) utilizing highly conductive CNTs as a high speed pathway for electron and ion transportation. It is then necessary to prove that the enhanced capacity due to the reversible conversion reaction really arose from the better electrochemical reaction kinetics associated with the above features. In addition, the relationship between the reaction kinetics and Na storage mechanisms needs to be fully understood to better design SnO_2 nanostructures.

The aforementioned obvious anodic peak in the CV curves (Fig. 4a) representing the reversible conversion reaction signifies the enhanced Na ion storage capacity of the A-SnO_2/CNT electrode. The anodic peak corresponds to strong reaction kinetics, such as fast Na ion diffusion rates, as in LIBs.[57]

To elucidate the electrochemical kinetics of the conversion reactions, CVs in the broad scan rate range 0.5–5 mV s^{-1} were measured for both the A- and C-SnO_2/CNT cells.

The maximum anodic peak currents marked by the arrows in Fig. 5a and S7† are plotted as a function of the square root of the scan rate, as shown in Fig. 5b. Their linear relationships indicate an obvious diffusion-controlled reaction, where the Randles–Sevcik equation is applicable:[58,59]

$$I_P = (2.69 \times 10^5) n^{3/2} A D^{1/2} C v^{1/2} \quad (3)$$

where I_P is the peak current, n is the number of electrons transferred in the reaction, A is the surface area of the electrode, D is the diffusion coefficient, C is the concentration of Na ions in the electrode material, and v is the scan rate. Note that the same number of transfer electrons (n) was involved in both electrodes, thus the much higher slope ($s = 2.42$) for the A-SnO_2/CNT electrode than that ($s = 1.79$) for the C-SnO_2/CNT means a higher D value of Na ions in the former than the latter electrode.[49]

To obtain a better understanding of the electron/ion transfer resistance of the two electrodes, the EIS spectra were measured in the frequency range 0.1–10^5 Hz, as shown in Fig. 5c. The data were fitted to the equivalent circuit model consisting of the resistance of the electrolyte (R_s), the charge transfer resistance (R_{ct}) and the Warburg resistance (W), and these impedance parameters are summarized in Table 1. Benefiting from the uniform SnO_2 layer on the CNT surface, R_{ct} was significantly lower for the A-SnO_2/CNT electrode than the C-SnO_2/CNT counterpart. This observation is in agreement with the electrical conductivities of the anode materials measured using the four probe method.

Furthermore, the EIS data in the low frequency range were used to calculate the Na ion diffusion coefficient, D_{Na}, according to eqn (4):

$$D_{Na} = \frac{R^2 T^2}{2A^2 n^4 F^4 C^2 \sigma^2} \quad (4)$$

where R is the gas constant, T is the temperature, F is the Faraday constant, and σ is the Warburg factor which can be

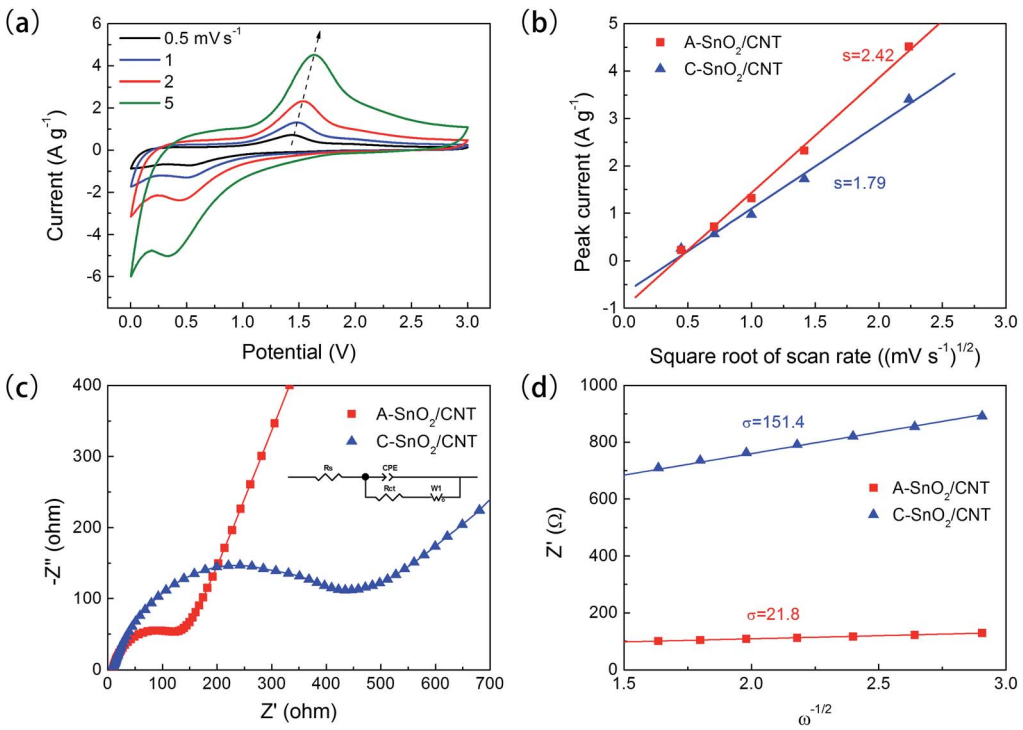

Fig. 5 (a) CV curves of the A-SnO_2/CNT electrode at different scan rates of 0.5, 1, 2 and 5 mV s^{-1}; (b) anodic peak current *versus* square root of the scan rate; (c) electrochemical impedance spectra (EIS) of the A- and C-SnO_2/CNT anodes; (d) resistance of Z' *versus* minus square root of the scanning frequency, ω, in the low frequency range of the EIS spectra.

Table 1 Comparison of resistance, electrical conductivity and ion diffusion coefficient between the A-SnO_2/CNT and C-SnO_2/CNT composites

	A-SnO_2/CNT	C-SnO_2/CNT
Solution resistance R_s (Ω)	9.9	9.7
Charge transfer resistance R_{ct} (Ω)	121.5	456.9
Electrical conductivity (S cm^{-1})	4.6×10^{-1}	2.7×10^{-2}
Na ion diffusion coefficient D_{Na} (cm^2 s^{-1})	5.94×10^{-17}	1.23×10^{-18}

taken directly from the slope of the linear plot of the real impedance (Z') against the minus square root of the frequency (Fig. 5d).[60,61] It is worth noting that the diffusion coefficient, D_{Na}, was about 50 times higher in the amorphous electrode than in the crystalline counterpart, *i.e.* 5.94×10^{-17} *vs.* 1.23×10^{-18} cm^2 s^{-1}, respectively (Table 1). It follows then that the much lower R_{ct} of the mainly amorphous SnO_2/CNT composite was a reflection of both the higher electronic conductivity and the higher D_{Na} than the crystalline counterpart, which in turn gave rise to a superior Na ion conversion reaction. This also means that Na ion diffusion is a limiting factor for the conversion reaction, and that a superior electrochemical performance of SnO_2-based anodes can be achieved by facilitating the full conversion reaction through enhanced Na ion diffusion kinetics.

3.4 *In situ* TEM analysis of structure evolution

The practical specific capacities of the SnO_2 anodes were far lower than their theoretical capacity in SIBs due to the aforementioned lack of alloying reaction and generally slow Na ion diffusion rate. To clarify the reasons behind the above observation, an in-depth understanding of the sodiation/desodiation phase change and a direct observation of the Na ion diffusion in the electrode is necessary. Several previous studies have partially revealed the phase changes of nanosized SnO_2 in SIBs through various *ex situ* characterizations.[20,27,28,62] However, inaccurate or incomplete information was often obtained due to unwanted changes occurring during sample preparation for *ex situ* experiments using active sodiated electrodes.[63] Indeed, it is challenging to identify real-time morphological changes using *ex situ* methods. Inspired by the pioneering *in situ* investigation of neat SnO_2 nanowires,[38,64] herein, the reaction mechanisms of

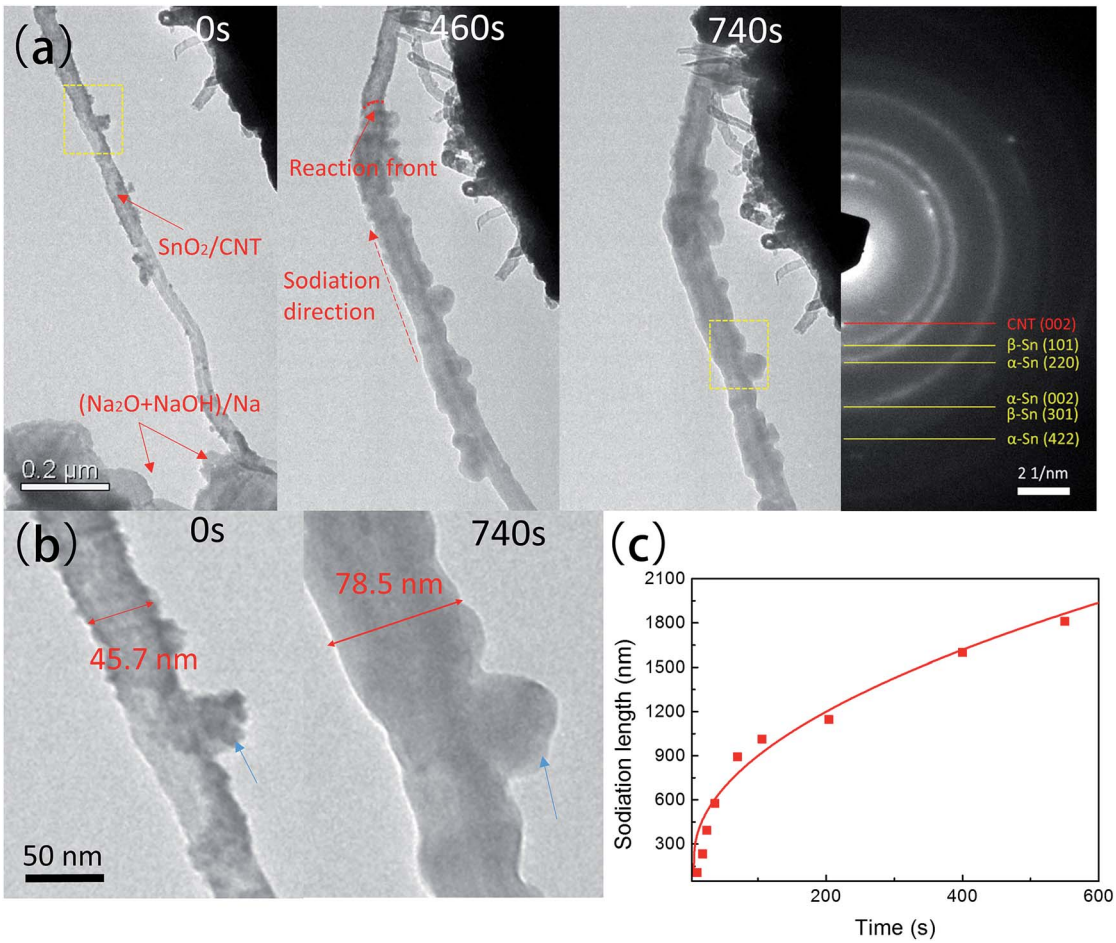

Fig. 6 Sequential TEM images of the A-SnO_2/CNT electrode taken from video frames: (a) change in the morphology during the initial sodiation process with the SAED pattern after sodiation, inset; (b) enlarged images of the yellow rectangles in (a); (c) progressive increase in sodiation length *vs.* sodiation time during the 1st sodiation process.

the SnO_2/CNT composite electrode and the roles that the CNT substrate played in enhancing the diffusion rate were *in situ* probed using TEM as follows. Fig. S8† schematically illustrates the *in situ* TEM setup within a TEM chamber. The TEM images taken during the initial sodiation process are shown in Fig. 6, while the full video is presented in ESI Movie 1.† When −2 V was applied to the electrode tip, the Na ions started to diffuse through the electrode axial direction, as marked by the red arrow (Fig. 6a). SnO_2 started to react with Na ions by the conversion reaction (eqn (1)), resulting in the formation of Sn crystals embedded in the Na_2O matrix with the associated expansion of the electrode diameter. The diffraction rings of Sn in the SAED taken after full sodiation (inset of Fig. 6a) further proved the Na ion storage in SnO_2 by conversion reaction, consistent with the conclusion drawn from the above CV and *ex situ* XRD results.[20,36]

The volume expansion taking place when Sn reacted with Na ions to form $Na_{15}Sn_4$ based on the alloying reaction was measured to be 420% according to a previous study.[37] However, the volume expansion of the A-SnO_2/CNT electrode should be lower than the above value. There are several reasons for this observation: namely, (i) the alloying reaction seldom occurs; (ii) the final product of the reaction is Sn, instead of $Na_{15}Sn_4$; and (iii) the CNTs can serve as a buffer to accommodate the volume expansion of SnO_2. The images in Fig. 6b present the enlarged diameter of the A-SnO_2/CNT electrode from 45.7 to 78.5 nm after full sodiation, equivalent to a volume expansion of ~195%, assuming a negligible change in electrode length. This value is much lower than 420%,[37] further confirming that only the conversion reaction took place. The reduced volume expansion supplies direct evidence for the better cyclic stability of the A-SnO_2/CNT electrode in SIBs.

To illustrate the Na ion diffusion through the A-SnO_2/CNT electrode, the positions of the reaction front were continuously monitored as a function of time, and the results are plotted in Fig. 6c. The sodiation length rapidly increased before it became rather saturated after 100 s, approximately following the rule of parabolic kinetics and indicating a diffusion-controlled reaction process.[38,64] This conclusion agrees well with the above reaction kinetics study based on the CV curves (Fig. 5b). Furthermore, it is interesting to note that the average sodiation speed of the SnO_2/CNT composite electrode was 3.2 nm s^{-1}, almost 6 times that of the neat SnO_2 electrode reported previously.[38] It appears that the presence of CNTs with a fine core/shell structure accelerated the reaction kinetics by overcoming the limitation of the relatively low Na ion diffusion coefficient.

4. Conclusions

SnO_2/CNT composites consisting of a mainly amorphous SnO_2 phase deposited on a CNT substrate were synthesized as anodes for SIBs. Their Na ion storage behaviors and corresponding reaction mechanisms are specifically studied using real-time *in situ* TEM and *ex situ* XRD analysis. The following can be highlighted from the study.

(i) The major Na ion storage capacity of the SnO_2 anodes arose from the reversible conversion reaction between SnO_2 and the Na ions to form metallic Sn upon full discharge.

(ii) A prominent anodic CV peak at 1.35 V was observed for the first time in SIBs, which corresponds to the reversible conversion reaction in (i).

(iii) The Na ion storage kinetics study revealed that slow Na ion diffusion limited the conversion reactions of SnO_2.

(iv) The small particle size and enlarged *d*-spacing arising from the mainly amorphous state of SnO_2 together with the conductive CNT substrate significantly enhanced the diffusion rate of Na ions to overcome the aforementioned kinetic limitations. As a result, the A-SnO_2/CNT electrode exhibited a superior specific capacity of 630.4 mA h g^{-1} at 0.1 A g^{-1} and 324.1 mA h g^{-1} at a high rate of 1.6 A g^{-1}.

Acknowledgements

This research project was financially supported by the Research Grants Council (GRF projects 613612 and 16212814) and the Innovation and Technology Commission (ITF project ITS/318/14) of Hong Kong SAR. The authors also appreciate the technical assistance from the Advanced Engineering Materials Facilities (AEMF) and the Materials Characterization and Preparation Facilities (MCPF) at HKUST.

References

1 J. M. Tarascon and M. Armand, *Nature*, 2001, **414**, 359.
2 M. Armand and J.-M. Tarascon, *Nature*, 2008, **451**, 652.
3 H. Pan, Y.-S. Hu and L. Chen, *Energy Environ. Sci.*, 2013, **6**, 2338.
4 M. D. Slater, D. Kim, E. Lee and C. S. Johnson, *Adv. Funct. Mater.*, 2013, **23**, 947.
5 B. L. Ellis and L. F. Nazar, *Curr. Opin. Solid State Mater. Sci.*, 2012, **16**, 168.
6 V. Palomares, P. Serras, I. Villaluenga, K. B. Hueso, J. Carretero-González and T. Rojo, *Energy Environ. Sci.*, 2012, **5**, 5884.
7 Z. Jian, L. Zhao, H. Pan, Y.-S. Hu, H. Li, W. Chen and L. Chen, *Electrochem. Commun.*, 2012, **14**, 86.
8 Z. Jian, W. Han, X. Lu, H. Yang, Y.-S. Hu, J. Zhou, Z. Zhou, J. Li, W. Chen, D. Chen and L. Chen, *Adv. Energy Mater.*, 2013, **3**, 156.
9 Y. Cao, L. Xiao, M. L. Sushko, W. Wang, B. Schwenzer, J. Xiao, Z. Nie, L. V. Saraf, Z. Yang and J. Liu, *Nano Lett.*, 2012, **12**, 3783.
10 S. Komaba, W. Murata, T. Ishikawa, N. Yabuuchi, T. Ozeki, T. Nakayama, A. Ogata, K. Gotoh and K. Fujiwara, *Adv. Funct. Mater.*, 2011, **21**, 3859.
11 R. Alcántara, J. M. Jiménez-Mateos, P. Lavela and J. L. Tirado, *Electrochem. Commun.*, 2001, **3**, 639.
12 S.-W. Kim, D.-H. Seo, X. Ma, G. Ceder and K. Kang, *Adv. Energy Mater.*, 2012, **2**, 710.
13 D. A. Stevens and J. R. Dahn, *J. Electrochem. Soc.*, 2000, **147**, 1271.

14 H. Zhu, Z. Jia, Y. Chen, N. Weadock, J. Wan, O. Vaaland, X. Han, T. Li and L. Hu, *Nano Lett.*, 2013, **13**, 3093.
15 J. S. Chen and X. W. D. Lou, *Small*, 2013, **9**, 1877.
16 H. Kang, Y. Liu, K. Cao, Y. Zhao, L.-F. Jiao, Y. Wang and H. Yuan, *J. Mater. Chem. A*, 2015, **3**, 17899.
17 X. Xie, S. Chen, B. Sun, C. Wang and G. Wang, *ChemSusChem*, 2015, **8**, 2948.
18 M. Dirican, Y. Lu, Y. Ge, O. Yildiz and X. Zhang, *ACS Appl. Mater. Interfaces*, 2015, **7**, 18387.
19 X. Zhao, Z. Zhang, F. Yang, Y. Fu, Y. Lai and J. Li, *RSC Adv.*, 2015, **5**, 31465.
20 Y. C. Lu, C. Ma, J. Alvarado, T. Kidera, N. Dimov, Y. S. Meng and S. Okada, *J. Power Sources*, 2015, **284**, 287.
21 Z. Li, J. Ding, H. Wang, K. Cui, T. Stephenson, D. Karpuzov and D. Mitlin, *Nano Energy*, 2015, **15**, 369.
22 H. Zhang, P. Xu, Y. Ni, H. Geng, G. Zheng, B. Dong and Z. Jiao, *J. Mater. Res.*, 2014, **29**, 617.
23 Y. Zhao, C. Wei, S. Sun, L. P. Wang and Z. J. Xu, *Adv. Sci.*, 2015, **2**, 1500097.
24 Y. Liu, X. Fang, M. Ge, J. Rong, C. Shen, A. Zhang, H. A. Enaya and C. Zhou, *Nano Energy*, 2015, **16**, 399.
25 D. Su, H.-J. Ahn and G. Wang, *Chem. Commun.*, 2013, **49**, 3131.
26 Y. Wang, D. Su, C. Wang and G. Wang, *Electrochem. Commun.*, 2013, **29**, 8.
27 J. Ding, Z. Li, H. Wang, K. Cui, A. Kohandehghan, X. Tan, D. Karpuzov and D. Mitlin, *J. Mater. Chem. A*, 2015, **3**, 7100.
28 J. Górka, L. Baggetto, J. K. Keum, S. M. Mahurin, R. T. Mayes, S. Dai and G. M. Veith, *J. Power Sources*, 2015, **284**, 1.
29 Y.-X. Wang, Y.-G. Lim, M.-S. Park, S.-L. Chou, J. H. Kim, H.-K. Liu, S.-X. Dou and Y.-J. Kim, *J. Mater. Chem. A*, 2014, **2**, 529.
30 Y. Zhang, J. Xie, S. Zhang, P. Zhu, G. Cao and X. Zhao, *Electrochim. Acta*, 2015, **151**, 8.
31 L. D. Ellis, T. D. Hatchard and M. N. Obrovac, *J. Electrochem. Soc.*, 2012, **159**, A1801.
32 J. Park, J.-W. Park, J.-H. Han, S.-W. Lee, K.-Y. Lee, H.-S. Ryu, K.-W. Kim, G. Wang, J.-H. Ahn and H.-J. Ahn, *Mater. Res. Bull.*, 2014, **58**, 186.
33 X. W. Guo, X. P. Fang, Y. Sun, L. Y. Shen, Z. X. Wang and L. Q. Chen, *J. Power Sources*, 2013, **226**, 75.
34 Y. Zhao, J. Li, N. Wang, C. Wu, G. Dong and L. Guan, *J. Phys. Chem. C*, 2012, **116**, 18612.
35 D. Su, C. Wang, H. Ahn and G. Wang, *Phys. Chem. Chem. Phys.*, 2013, **15**, 12543.
36 Z. Li, J. Ding and D. Mitlin, *Acc. Chem. Res.*, 2015, **48**, 1657.
37 J. W. Wang, X. H. Liu, S. X. Mao and J. Y. Huang, *Nano Lett.*, 2012, **12**, 5897.
38 M. Gu, A. Kushima, Y. Shao, J. G. Zhang, J. Liu, N. D. Browning, J. Li and C. Wang, *Nano Lett.*, 2013, **13**, 5203.
39 X.-M. Liu, Z. D. Huang, S. W. Oh, B. Zhang, P.-C. Ma, M. M. F. Yuen and J.-K. Kim, *Compos. Sci. Technol.*, 2012, **72**, 121.
40 J. G. Zhou, H. T. Fang, J. M. Maley, J. Y. P. Ko, M. Murphy, Y. Chu, R. Sammynaiken and T. K. Sham, *J. Phys. Chem. C*, 2009, **113**, 6114.
41 Y. Jia, P.-Y. Wu, Y.-P. Jiang, Q.-Y. Zhang, S.-S. Zhou, F. Fang and D.-Y. Peng, *New J. Chem.*, 2014, **38**, 1100.
42 Y. Zheng, T. Zhou, C. Zhang, J. Mao, H. Liu and Z. Guo, *Angew. Chem., Int. Ed.*, 2016, **55**, 3408.
43 X.-M. Liu, Z.-D. Huang, S. Oh, P.-C. Ma, P. C. H. Chan, G. K. Vedam, K. Kang and J.-K. Kim, *J. Power Sources*, 2010, **195**, 4290.
44 Z.-L. Xu, B. Zhang, Y. Gang, K. Cao, M. Akbari Garakani, S. Abouali, J. Huang, J.-Q. Huang, E. Kamali Heidari, H. Wang and J.-K. Kim, *Energy Storage Materials*, 2015, **1**, 25.
45 L. Jiang, G. Sun, Z. Zhou, S. Sun, Q. Wang, S. Yan, H. Li, J. Tian, J. Guo, B. Zhou and Q. Xin, *J. Phys. Chem. B*, 2005, **109**, 8774.
46 H. Zhu, D. Yang, G. Yu, H. Zhang and K. Yao, *Nanotechnology*, 2006, **17**, 2386.
47 Z. Wang, G. Chen and D. Xia, *J. Power Sources*, 2008, **184**, 432.
48 H.-T. Fang, X. Sun, L.-H. Qian, D.-W. Wang, F. Li, Y. Chu, F.-P. Wang and H.-M. Cheng, *J. Phys. Chem. C*, 2008, **112**, 5790.
49 B. Zhang, Y. Yu, Z. Huang, Y.-B. He, D. Jang, W.-S. Yoon, Y.-W. Mai, F. Kang and J.-K. Kim, *Energy Environ. Sci.*, 2012, **5**, 9895.
50 B. Zhang, J. Huang and J.-K. Kim, *Adv. Funct. Mater.*, 2015, **25**, 5222.
51 Y. Caglar, S. Ilican and M. Caglar, *Eur. Phys. J. B*, 2007, **58**, 251.
52 A. Lopez-Rubio, B. M. Flanagan, E. P. Gilbert and M. J. Gidley, *Biopolymers*, 2008, **89**, 761.
53 D. Barreca, *Surf. Sci. Spectra*, 2000, **7**, 81.
54 P. C. Ma, J.-K. Kim and B. Z. Tang, *Carbon*, 2006, **44**, 3232.
55 V. Datsyuk, M. Kalyva, K. Papagelis, J. Parthenios, D. Tasis, a. Siokou, I. Kallitsis and C. Galiotis, *Carbon*, 2008, **46**, 833.
56 M. Okubo, E. Hosono, J. Kim, M. Enomoto, N. Kojima, T. Kudo, H. Zhou and I. Honma, *J. Am. Chem. Soc.*, 2007, **129**, 7444.
57 B. Zhang, Y. Liu, Z. Huang, S. Oh, Y. Yu, Y.-W. Mai and J.-K. Kim, *J. Mater. Chem.*, 2012, **22**, 12133.
58 C. O. Laoire, S. Mukerjee, K. M. Abraham, E. J. Plichta and M. A. Hendrickson, *J. Phys. Chem. C*, 2009, **113**, 20127.
59 Y. Shi, L. Wen, F. Li and H.-M. Cheng, *J. Power Sources*, 2011, **196**, 8610.
60 M. Park, X. Zhang, M. Chung, G. B. Less and A. M. Sastry, *J. Power Sources*, 2010, **195**, 7904.
61 J. Sun, L. Xiao, S. Jiang, G. Li, Y. Huang and J. Geng, *Chem. Mater.*, 2015, **27**, 4594.
62 A. Jahel, C. M. Ghimbeu, A. Darwiche, L. Vidal, S. Hajjar, C. Vix-Guterl and L. Monconduit, *J. Mater. Chem. A*, 2015, **3**, 11960.
63 K. He, S. Zhang, J. Li, X. Yu, Q. Meng, Y. Zhu, E. Hu, K. Sun, H. Yun, X.-Q. Yang, Y. Zhu, H. Gan, Y. Mo, E. A. Stach, C. B. Murray and D. Su, *Nat. Commun.*, 2016, **7**, 11441.
64 J. Y. Huang, L. Zhong, C. M. Wang, J. P. Sullivan, W. Xu, L. Q. Zhang, S. X. Mao, N. S. Hudak, X. H. Liu, A. Subramanian, H. Fan, L. Qi, A. Kushima and J. Li, *Science*, 2010, **330**, 1515.